Energy Conversion and Management 342 (2025) 120096

Contents lists available at ScienceDirect

Energy Conversion and Management

journal homepage: www.elsevier.com/locate/enconman

Pyrolysis kinetics of organic matter in oil shale: A modeling method and its application to the oil shale in the Chang7$_3$ Submember of the Triassic Yanchang Formation, Ordos Basin

Chi Xiong, Jingyu Chen, Ruina Xu, Qiang Song [*,1]

Key Laboratory of Thermal Science and Power Engineering of Ministry of Education, Department of Energy and Power Engineering, Tsinghua University, 100084 Beijing, China

ARTICLE INFO

Keywords:
Oil Shale
In-situ Conversion
Peak Deconvolution
Organic Matter Pyrolysis
Kinetic Model
Product Distribution

ABSTRACT

The in-situ conversion is a promising technology for extracting medium–low maturity shale oil, involving a multiple reaction-coupled pyrolysis process. A kinetic model that predicts the pyrolysis process and product distributions is crucial for the development of in-situ conversion technology. This study presents a method to build a multi-step kinetic model and applies it to the pyrolysis of oil shale in the Chang7$_3$ submember of the Triassic Yanchang Formation (OSC7$_3$). Thermogravimetric analyses at heating rates of 0.2–4 °C/min were conducted to investigate the pyrolysis characteristics of the OSC7$_3$ between 50–750 °C. The process exhibited the characteristics of coupled multiple reactions above 330 °C. Through peak deconvolution and activation energy distribution analysis, the pyrolysis of OSC7$_3$ was decoupled into water evaporation and six distinct reactions. Staged isothermal pyrolysis experiments showed that most oil and gas were produced during the organic matter pyrolysis stage. Based on the product characterization, this stage was divided into four reactions (the conversion of kerogen, primary cracking, secondary cracking, and tertiary cracking of bitumen), and the product distribution of each reaction was determined. Kinetic analysis for each reaction was performed based on the deconvoluted results of thermogravimetric analyses at heating rates of 0.5–4 °C/min. A multi-reaction kinetic model was developed, which demonstrates a good prediction accuracy for the pyrolysis of organic matter in OSC7$_3$. Due to the precise decoupling of multiple reactions, the kinetic model can be successfully applied to a slower heating process (0.2 °C/min), which is important for guiding the design and optimization of in-situ conversion technology.

1. Introduction

The extraction of medium–low maturity shale oil is crucial for ensuring the long-term stability of the national petroleum industry and energy security [1]. In recent years, China has made breakthroughs in exploring medium–low maturity shale oil resources, necessitating the establishment of efficient extraction technologies for effective production from such reservoirs [2–4]. Medium-low maturity shale oil refers to the heavy oils, thermal bitumen, and unconverted solid organic matter (kerogen) within oil shale. Due to its depth and solid form, conventional fracturing and ground retorting technologies are no longer applicable. Shell, in collaboration with the China National Petroleum Exploration and Development Research Institute, proposed in-situ conversion technology (ICP), which involves continuous heating of the oil shale layers to convert organic matter into light oil and gas for extraction [1,3,5,6]. The choice of heating rate and temperature are crucial as they determine both the heating cost and the composition of the oil and gas products, significantly influencing the economic viability of extraction. The rational design of the heating process and temperature needs the support of a reliable in-situ conversion kinetics model of oil shale.

In-situ conversion of oil shale primarily involves pyrolysis under a controlled heating process. Therefore, thermogravimetric analysis (TGA) is commonly used to study the pyrolysis characteristic of oil shale, with the TGA results serving as the basis for developing kinetic models.

* Corresponding author.
E-mail addresses: Xiongc22@mails.tsinghua.edu.cn (C. Xiong), jingyu-c20@mails.tsinghua.edu.cn (J. Chen), ruinaxu@tsinghua.edu.cn (R. Xu), qsong@tsinghua.edu.cn (Q. Song).
[1] Researcher ID: U-4938-2019.

https://doi.org/10.1016/j.enconman.2025.120096
Received 5 January 2025; Received in revised form 26 May 2025; Accepted 17 June 2025
Available online 25 June 2025

Since oil shale is mainly used for oil production through pyrolysis, the focus is on the organic matter pyrolysis stage. Existing studies indicate considerable variability in the pyrolysis characteristic of oil shales from different sources, owing to compositional differences [7–14]. Due to laboratory constraints, TGA is often conducted at relatively high heating rates (above 10 °C/min), where most oil shales exhibit a single weight loss peak during the organic matter cracking stage. As a result, this stage is often modeled as a single reaction for kinetic analysis, which yields good fitting results [9,13,15–17]. However, some oil shales show overlapping weight loss peaks during the organic matter cracking stage [18–20], indicating the coupling of multiple reactions. In practical in-situ conversion processes, the heating rate is very slow(0.8-1000 °C/day) [21], which causes the previously coupled multiple reactions to be separated. A kinetic model based on the assumption of a single overall reaction may lead to significant prediction errors [22,23]. Therefore, decoupling multiple reactions is essential when developing a kinetic model for in-situ conversion of oil shale to ensure the model's applicability to underground heating processes.

Some researchers have attempted to decouple the pyrolysis process of oil shale using the peak deconvolution method [24], separating overlapping peaks into multiple single weight loss peaks through various peak shape functions. Each peak is treated as an independent reaction [18,25,26], the weight loss characteristics of which can be represented by the peak shape and location. Bai [18] applied this method to the organic matter cracking stage of Huadian oil shale, using two fitted peaks, and found that fitting accuracy significantly improved compared to single-peak fitting. He concluded that the stage involved two reactions: the volatilization of free bitumen and kerogen cracking. Ding [25] conducted TGA on Fushun oil shale and used peak deconvolution method based on fitting accuracy. He proposed a three-step mechanism: weak bond cracking in kerogen, followed by bitumen formation, and then the breaking of aliphatic chains and aromatic carbon in bitumen. However, these studies rely on fitting accuracy to determine the peak positions and shapes, which does not fully ensure that each weight loss peak corresponds to an independent reaction. For example, in Bai's study [18], the activation energy for each fitted peak was calculated using the *iso*-conversional methods, and it was found that for the studied oil shale, the activation energy varied by more than 40 % as the conversion increased from 0.1 to 0.9. This contradicts the characteristic that activation energy for a distinct reaction should remain consistent over a wide conversion range. Similar issues were found in biomass studies [27–29]. To address these issues, our team improved the peak deconvolution method by adding an activation energy distribution criterion based on fitting accuracy. This ensures that the deconvolution results not only have high fitting accuracy but also that the relative average deviation of activation energy for each peak remains below 10 % across the conversion range. This guarantees that each fitted peak corresponds to an independent reaction [30]. Due to the limitations of the existing peak deconvolution method in decoupling accuracy, the kinetic models derived from the deconvolution results contain errors. Furthermore, most current kinetic models are based on TGA results, which describe the weight loss during pyrolysis but do not address product distribution. As a result, these models lack the ability to predict the generated products. Therefore, it is necessary to conduct studies on the distribution of pyrolysis products alongside developing kinetic models.

The composition of oil shale pyrolysis products is typically determined through pyrolysis experiments combined with product characterization. The heating process usually involves rapidly heating multiple samples from ambient temperature to different temperature points, followed by characterization of the pyrolysis products at each stage. The reaction process between temperature points is inferred based on the differences in product distributions. Zhang [31] rapidly heated Gonghe oil shale from ambient temperature to 470, 520, and 600 °C (15 s for each temperature step). By subtracting the product distributions at each temperature, it was inferred that before 470 °C, the kerogen's heteroatom functional groups broke down and converted to bitumen, followed by the primary and secondary cracking of aliphatic compounds in bitumen between 470–520 °C and 520–600 °C. You [32] used a fixed-bed pyrolysis system to heat four sets of Dachengzi oil shale to 430, 460, 490, and 520 °C—temperature points corresponding to different stages of organic matter pyrolysis. Based on differences in product distributions and gas composition of each stage, it was inferred that at these temperature points, the cracking and dehydrogenation of aliphatic hydrocarbons, the cleavage of aliphatic chains near the aromatic rings, and the breaking of heteroatomic bonds near the aromatic rings occurred sequentially. Other scholars have used similar methods to study the product distributions and reaction pathways of specific oil shales [20,33,34]. This method can reveal the pyrolysis product composition within different temperature ranges and help infer the reaction pathways. However, when the heating rate is fast during temperature-programmed pyrolysis, the coupling of reactions intensifies, and the temperature overlap range increases. As a result, the product distributions obtained may represent the cumulative result of multiple coupled reactions. Moreover, existing methods lack a clear basis for selecting experimental temperature points, which makes it impossible to ensure a one-to-one correspondence between experimental temperature and distinct reactions. Thus, it is difficult to systematically obtain the pyrolysis products of each reaction. In our previous work, we proposed a method that accurately identifies the pyrolysis products of each reaction [30]. By using peak deconvolution to decouple multiple pyrolysis processes and determining the peak temperatures for each reaction, we conducted staged isothermal pyrolysis experiments at each temperature point. This approach allows for the precise identification of product compositions for each reaction and offers a feasible solution for comprehensively understanding the multi-step pyrolysis mechanism of oil shale.

Establishing an accurate kinetic model to describe the pyrolysis process of oil shale is crucial for guiding the development of in-situ conversion technology. Existing studies face challenges in decoupling the pyrolysis process and characterizing the products of distinct reactions, making their kinetic models unsuitable for the extremely slow heating process (typical of in-situ conversion). Furthermore, most current kinetic models are based on TGA results, lacking the ability to predict the generated products of oil shale. This study proposes a method for establishing a multi-reaction kinetic model and successfully applies it to the $OSC7_3$, which is a significant source of China's medium-to-low maturity shale oil. First, TGA was used to identify the pyrolysis weight loss characteristic of $OSC7_3$ during the temperature-programmed process. Using the peak deconvolution method, the oil shale pyrolysis process was decoupled precisely, and the weight loss characteristics of each distinct reaction were obtained. Based on this, staged isothermal pyrolysis experiments were conducted using a fixed-bed reactor, and the products of each reaction were collected and characterized to analyze their composition and reaction pathways. Finally, kinetic analysis was performed based on the peak deconvolution results and pyrolysis product distributions, resulting in the distribution range and initial values of the kinetic triplet parameters, which were optimized to obtain the oil shale organic matter pyrolysis kinetic model (OMPM). This kinetic model not only accurately predicts the pyrolysis characteristics of oil shale organic matter under various heating profiles, but also provides the temporal distribution of pyrolysis products, offering significant guidance for the application of in-situ conversion technology to exploit the $OSC7_3$.

2. Experimental

2.1. Sample preparation

The oil shale samples used in this study were sourced from the Maquan section in the $Chang7_3$ submember of the Triassic Yanchang Formation in the Ordos Basin. The total organic carbon (TOC) content

ranged from 12.91 % to 15.53 %, with an average value of 14.23 %. The kerogen is primarily of Type I or Type II_1. Further details about the samples can be found in [35]. The samples were prepared in accordance with the Chinese standard for coal sample preparation (GB/T 474–2008). The bulk oil shale was crushed into a 60-mesh powder and then dried in an air-circulated drying oven for 12 h at 50 °C. The prepared samples were sealed for subsequent experiments. Elemental analysis and proximate analysis data for the oil shale samples are provided in Table 1.

2.2. Thermogravimetric analysis and deconvolution method

Approximately 10 mg of oil shale powder was used for thermogravimetric analysis (TGA, TGA/DSC3+, Mettler Toledo) under a temperature-programmed heating procedure from 50 °C to 750 °C. Before 300 °C, the process was primarily physical water evaporation, with a heating rate of 20 °C/min. Subsequently, the samples were heated at rates of 0.2, 0.5, 1, 2, and 4 °C/min up to 750 °C. All experiments were performed under a nitrogen atmosphere with a flow rate of 50 ml/min. In the establishment of the kinetic model, only the experimental results at heating rates of 0.5–4 °C/min were used, while the result at a heating rate of 0.2 °C/min was used to validate the model's predictive ability for the pyrolysis process at slower heating rates.

Based on the above experiments, the DTG curves of the sample exhibited overlapping weight loss peaks after 330 °C, corresponding to the organic matter pyrolysis stage and the mineral pyrolysis stage [8,12]. To achieve the decoupling of the multiple reaction process, the overlapping peak regions of the DTG curve were separated using the peak deconvolution method. First, a mathematical function $F(T)$ with peak characteristics was selected. Based on literature findings, different numbers of fitting peaks (representing reactions) were used to fit the overlapping peak regions. The fitting accuracy was compared for different numbers of peaks, and the three fitting peaks with the highest accuracy were selected. Then, based on the activation energy distributions, the optimal decoupling scheme was determined: the *iso*-conversional method was used to investigate the activation energy distributions of each weight loss peak in the conversion range of 0.1–0.9 for different decoupling scheme. The fitting peak number that resulted in no significant fluctuation in the activation energy across the conversion range was selected as the final decoupling result. This determined the specific reaction number for the multiple reaction process and obtained the pyrolysis weight loss characteristics for each reaction. Based on the peak temperatures of these weight loss peaks, staged isothermal pyrolysis experiments can be adopted to collect and characterize the products of each reaction, enabling the analysis of product distributions and the inference of reaction mechanisms. Moreover, the pyrolysis weight loss characteristics of each reaction under different heating rates can be used to establish kinetic models of corresponding reactions. These results enable the establishment of the OMPM. The specific peak deconvolution method can be found in [30]. The activation energy calculation method used was the Starink (STK) method [36]. The fitting accuracy was evaluated using the correlation coefficient R^2 and residual sum of squares (*RSS*).

2.3. Staged isothermal pyrolysis experiments on oil shale

2.3.1. Experimental system

The staged isothermal pyrolysis experiments of oil shale were conducted using the fixed-bed reactor system shown in Fig. 1 [30]. The reaction section of the fixed-bed reactor system is used to heat the oil shale samples. This section consists of an electric furnace, inner and outer quartz tubes, and a quartz plate. During experiments, the carrier gas (500 ml/min N_2) carries the pyrolysis products along the tubing. The oil and water products are collected by a cold trap, while the gas products are characterized online by Fourier transform infrared spectroscopy (FTIR) and subsequently collected in gas bags for later gas chromatography (GC) analysis. For detailed information about the system, refer to [30].

2.3.2. Experimental methods

To investigate the characteristics and mechanisms of each independent reaction, staged isothermal pyrolysis experiments were conducted on oil shale powder (particle size < 60 mesh) with an initial mass of 10 g (m_0). Following a temperature gradient from low to high, the sample was heated isothermally at each temperature point until the absorption peaks of various gases in the FTIR online detection results almost disappeared. The sample was then cooled to ambient temperature under N_2 protection. After collecting the pyrolysis products at this stage, the sample was reheated to the next temperature point for further isothermal pyrolysis, continuing the process until the final temperature point. The specific method is described in detail in [30]. Using this method, we obtained the solid product mass m_i, and the yields of water, oil, and gas products, m_{Wi}, m_{Oi}, m_{Gi}, where m is the mass of the oil sample at the current temperature, and the subscript i represents the i-th temperature point. The pyrolysis weight loss Y_{Li}, oil yield Y_{Oi}, water yield Y_{Wi}, and gas yield Y_{Gi} at the i-th temperature point during isothermal pyrolysis were calculated using **Eqs. (1)–(4)**.

$$Y_{Li} = \frac{m_{i-1} - m_i}{m_0} \times 100\% \tag{1}$$

$$Y_{Oi} = \frac{m_{Oi}}{m_0} \times 100\% \tag{2}$$

$$Y_{Wi} = \frac{m_{Wi}}{m_0} \times 100\% \tag{3}$$

$$Y_{Gi} = Y_{Li} - Y_{Wi} - Y_{Oi} \tag{4}$$

The mineral content of the oil shale samples after pyrolysis at each temperature point was examined using an X-ray diffractometer (XRD) (Rigaku, Japan, S2). Oil products from the staged isothermal pyrolysis experiments were analyzed using a gas chromatography/mass spectrometer (GC–MS) system (Shimadzu QP 2010) at each temperature stage. The gas products collected in bags were analyzed with a Gas Chromatograph (GC) (Agilent 8890). The FTIR (Thermo Scientific, Nicolet iS10) was used to characterize the online composition of oil shale gas products. Detailed procedures for the characterization techniques can be found in the supplementary materials.

2.4. Kinetic modeling

The pyrolysis process of $OSC7_3$ is decoupled into multiple parallel

Table 1
Proximate and ultimate analysis of $OSC7_3$ (on an air-dry base).

Proximate analysis[a] (wt%)				Ultimate analysis[a] (wt%)				
Moisture	Volatile matter	Ash	Fixed carbon	C	H	O	N	S
1.3540	13.4316	81.2514	3.9630	10.288	1.625	5.620	0.530	4.041

[a] As air-dried basis.

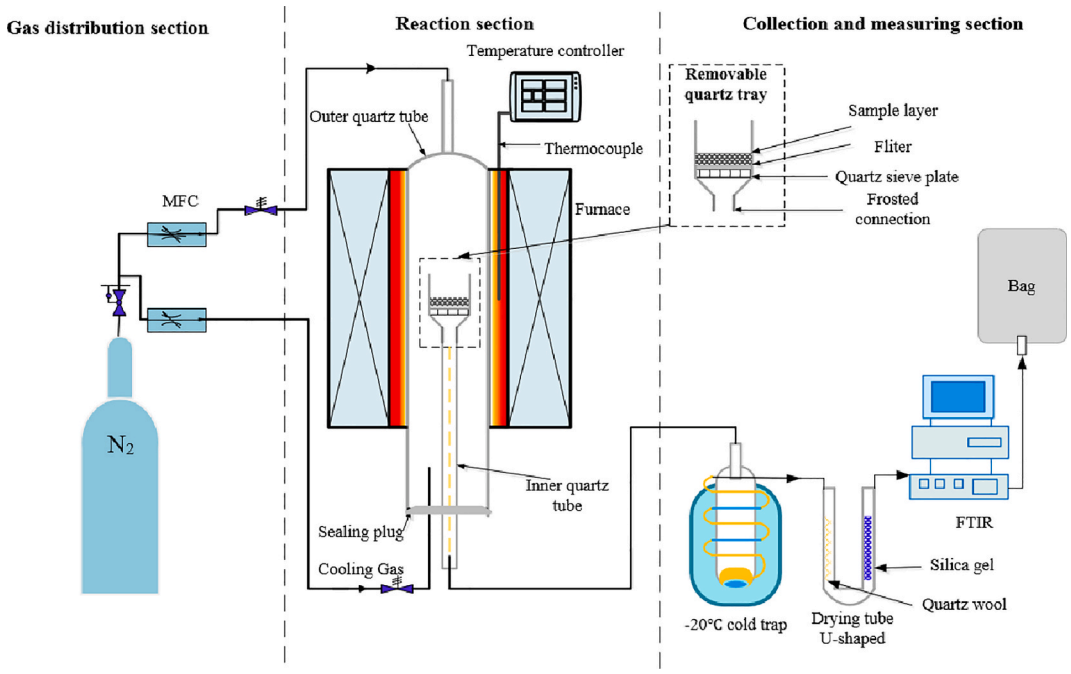

Fig. 1. The schematic diagram of the fixed-bed reactor system for oil shale pyrolysis.

independent reactions, with the rate equation for each reaction described as shown in **Eq. (5)**:

$$\frac{d\alpha_l}{dt} = \frac{1}{\beta}\frac{d\alpha_l}{dT} = A_l \exp^{(-E_l/RT)} f_l(\alpha_l) \tag{5}$$

The α represents the conversion, the subscript l represents the l-th reaction, t is the time, β is the heating rate (dT/dt), T is the temperature, R is the universal gas constant, and A, E, and $f(\alpha)$ are the kinetic triplet parameters, corresponding to the pre-exponential factor, activation energy, and the reaction model, respectively. To obtain accurate values for the three parameters, the calculated results based on **Eq. (5)** are compared with experimental data, and the kinetic parameters are

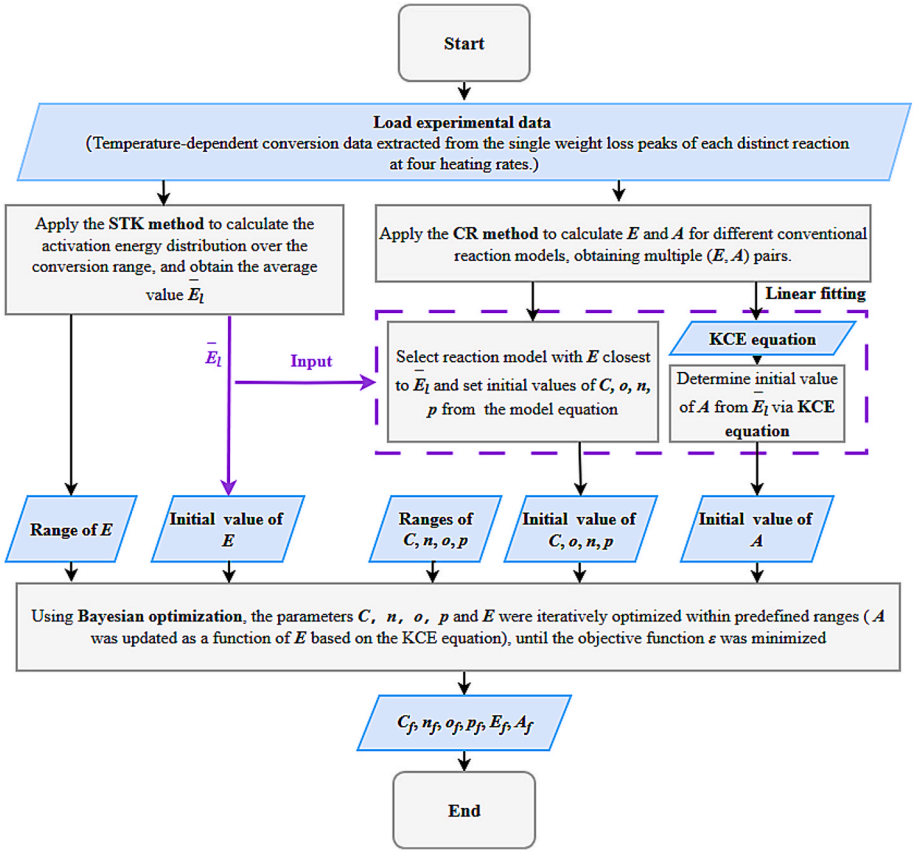

Fig. 2. Flowchart for determining kinetic parameters of each pyrolysis reaction during the pyrolysis phase of $OSC7_3$ organic matter.

iteratively optimized to minimize deviations. This process leads to the optimal parameter set with the best fitting accuracy. However, direct fitting is computationally intensive and time-consuming. Therefore, this study first used the STK method, Coats-Redfern (CR) method [37], and the kinetic compensation effects (KCE) to determine the distribution range and relatively accurate initial values of the kinetic parameters for each reaction. Subsequently, further optimization was carried out. This strategy can significantly reduce computation time. By combining the final kinetic equations for each reaction with the corresponding product compositions, we establish the OMPM. This model can predict both the pyrolysis process and the distributions of the resulting products. Detailed procedures can be found in Sections 2.4.1-2.4.2.

2.4.1. Determination of kinetic parameters for each reaction

From **Eq. (5)**, the calculation formula for the conversion α_l of each reaction can be derived as **Eq. (6)**, where T_0 represents the initial reaction temperature.

$$\alpha_l = \int_{T_0}^{T} \frac{\mathrm{d}\alpha_l}{\mathrm{d}T} = \int_{T_0}^{T} \frac{A_l}{\beta} \exp^{-E_l/RT} f_l(\alpha_l)\mathrm{d}T \tag{6}$$

Utilizing the weight loss peaks corresponding to each reaction of organic matter pyrolysis, along with **Eq. (6),** the conversion as a function of temperature at various heating rates was determined. These data form the basis for kinetic analysis, and the determination procedure for the kinetic parameters of each reaction is shown in Fig. 2.

After loading the experimental data, the first step is to determine the distribution range and initial value of the activation energy. In this work, the *iso*-conversional method is used to determine the activation energy distribution range and initial values of each reaction, as it only requires the reaction weight loss characteristics at different heating rates, without the need to pre-define a reaction model. Existing studies [29] have indicated that, compared to other *iso*-conversional methods [38,39], the STK method [36] has lower relative errors. Thus, the STK method is used to calculate the activation energy at different conversions. The calculation formula for the STK method is shown in **Eq. (7)**.

$$\ln\left(\frac{\beta}{T^{1.92}}\right) = Constant - 1.0008\frac{E(\alpha)}{RT} \tag{7}$$

At different heating rates, the temperature corresponding to the same conversion for the same reaction is selected. The activation energy $E(\alpha)$ at the current conversion can be obtained by fitting the slope of the straight line between $\ln(\beta / T^{1.92})$ and $1/T$. When calculating the reaction activation energy, the conversion range is taken as [0.1–0.9], with intervals of 0.1. The upper and lower limits of the activation energy within this conversion range can be used to determine the activation energy distribution range. The average value of the activation energy at 9 different conversions is taken as the initial value $\overline{E}_l$ for the reaction activation energy, which is then used to determine the corresponding reaction model and pre-exponential factor.

The reaction model then needs to be determined. Since the oil shale pyrolysis process is complex, in this study, the mathematical form of the reaction model is selected based on the research by the International Confederation for Thermal Analysis and Calorimetry (ICTAC) [24]. The mathematical form is shown in **Eq. (8)**, where C、o、n、p are the parameters to be determined.

$$f(\alpha) = C\alpha^{o}(1-\alpha)^{n}[-\ln(1-\alpha)]^{p} \tag{8}$$

It is generally assumed that the reaction order does not exceed 5 [9,17,41,42]. Based on this assumption and the existing mathematical forms of the traditional reaction models, the distribution ranges of the parameters within **Eq. (8)** are shown in Table 2.

Directly solving the reaction model equations parameters iteratively over the full parameter distribution range is computationally intensive. However, with different parameter values in **Eq. (8)**, it can transform into various traditional reaction models. Therefore, a suitable traditional mechanistic function can be initially selected, and its parameters used as the initial values for iteration to reduce computational time. The CR method is a valuable tool for obtaining the pre-exponential factor A and activation energy E corresponding to each traditional reaction model. If the activation energy calculated from a given reaction model is closest to the $\overline{E}_l$, this model is considered to represent the actual reaction mechanism relatively accurately compared to the other traditional reaction models, and its parameters can be adopted as the initial values for further iterative optimization. The mathematical form of the CR method is shown in **Eq. (9)**, where $g(\alpha)$ is the integral form of the reaction model $f(\alpha)$. Given the heating rate β and the reaction model $f(\alpha)$, the activation energy E at the current heating rate and reaction model can be determined by plotting $\ln(g(\alpha) / T^2)$ against $1/T$ and obtaining the slope of the fitted line. By substituting the existing traditional reaction models (Please refer to the supplementary materials **Table S1**), the corresponding activation energies can be obtained. The theoretical background of these reaction models can be found in other literature [40].

Table 2
Optimization range of the reaction model parameters.

Parameters	C	o	n	p
Search range	[0,5]	[-1, 1]	[-1, 5]	[-1, 1]

$$\ln\frac{g(\alpha)}{T^2} = \ln\left(\frac{AR}{\beta E}\right) - \frac{E}{RT} \tag{9}$$

The third step involves determining the distribution range and initial value of the pre-exponential factor A. For a given distinct reaction, the logarithmic form of the pre-exponential factor $\ln A$ is linearly correlated with the activation energy E [43,44]. This correlation is referred to as the kinetic compensation effect. Therefore, both the initial value and the optimized parameter value of the pre-exponential factor can be calculated based on the KCE and the corresponding activation energy at a given time, eliminating the need to define a range for the A. This relationship is expressed in **Eq. (10)**, where a and b represent the compensation parameters. By using the Coats-Redfern method, multiple sets of activation energy E and corresponding pre-exponential factors A can be obtained. These values are then linearly fitted to determine the slope (a) and intercept (b). To calculate the initial value of the pre-exponential factor, $\overline{E}_l$ is substituted into the equation to obtain the corresponding pre-exponential factor.

$$\ln(A_l) = \mathrm{a}_l\overline{E_l} + b_l \tag{10}$$

After determining the distribution range and initial values of the reaction kinetic parameters using the methods described above, further optimization is required. The six parameters to be optimized in the kinetic model are C, o, n, p, E, and A. Since the pre-exponential factor (A) is a function of the activation energy (E) based on the kinetic compensation effect, it is not considered an independent optimization parameter. Based on the obtained initial values of the six parameters, **Eqs. (5), (9), and (10)** are used to predict the conversion at different temperatures, which is then compared with experimental data to calculate the prediction error (i.e., the objective function). Next, the Bayesian optimization algorithm is used to iteratively search for the parameter direction that most effectively reduces the prediction error within the predefined parameter range. The parameters are iterated step-by-step, and the objective function is recalculated at each iteration. (After each iteration, the A is updated according to the E for the calculation of the objective function.) Finally, the kinetic model with the minimum prediction error within the set number of iterations is selected as the final result. The algorithm's objective function ε is shown in **Eq. (11)**, where k represents the k-th heating rate.

$$\varepsilon = \sum_{k}^{4} \sum_{j}^{99} (\alpha^{Exp} - \alpha^{Sim})^2 \tag{11}$$

The calculation process of the objective function is as follows: with a step size of 0.01, 99 temperature points corresponding to conversions ranging from 0.01 to 0.99 are determined. The kinetic parameters are used to predict the conversions at these temperatures. The sum of the absolute differences between the experimental and predicted conversions at these temperature points is taken as the prediction error for the kinetic model at a given heating rate. The total prediction error across the four heating rates is summed to form the objective function.

The performance of the kinetic model for each reaction can be evaluated by comparing the predicted conversion curves (as a function of temperature) with the experimental curves, using the correlation coefficient R^2. The experimental curves for each reaction can be obtained by the deconvolution results of the DTG curves.

2.4.2. Determination and evaluation of the kinetic model for oil shale organic matter pyrolysis

The conversion of oil shale organic matter is defined as the ratio of the current weight loss of organic matter to the total weight loss when the organic matter is fully reacted. In this study, the organic matter conversion α_{OM} during TG experiments was calculated using **Eq. (12)**, where the subscript *OM* represents organic matter, m_{Dry} is the oil shale mass after the moisture evaporation stage (corresponding to the oil shale mass at 300 °C during the TG experiments), and n represents the number of distinct reactions in the stage.

$$\alpha_{OM} = \frac{m_{Dry} - m}{m_0 \sum_{l=1}^{n} Y_l} \tag{12}$$

Since the pyrolysis of oil shale organic matter consists of multiple reactions, the organic matter conversion is related to the conversions of each distinct reaction. This relationship can be expressed using **Eq. (13)**. In this equation, w_l represents the weight fraction for each distinct reaction. The weight fractions for each reaction can be determined based on the ratio of the weight loss Y_l during that reaction to the total weight loss during the oil shale organic matter pyrolysis phase, which can be calculated using **Eq. (14)**.

$$\alpha_{OM} = \sum_{l=1}^{n} w_l \alpha_l \tag{13}$$

$$w_l = Y_l / \sum_{l=1}^{n} Y_l \tag{14}$$

To derive the kinetic model of oil shale organic matter pyrolysis, the differential of **Eq. (13)** with respect to temperature is taken, resulting in the kinetic model expressed by **Eq. (15)**. The accuracy of the model's prediction of the overall reaction process can be evaluated by comparing the experimental curves of organic matter conversion versus temperature with the model-predicted curves during the pyrolysis stage. The correlation coefficient R^2 between the experimental and predicted curves in the temperature range of the organic matter pyrolysis stage is used as a measure of the model's prediction accuracy.

$$\frac{d\alpha_{OM}}{dT} = \sum_{l=1}^{n} w_l \frac{d\alpha_l}{dT} \tag{15}$$

3. Result and discussion

3.1. Thermogravimetric analysis and deconvolution of $OSC7_3$

The TG/DTG curves of $OSC7_3$ pyrolyzed at four different heating rates are shown in Fig. 3. The mass loss rate is minimal (only 1 %) before 300 °C, which is typically attributed to the volatilization of free water and interlayer water in the mineral matrix of the oil shale [45,46]. The principal mass loss stage occurs between 300 °C and 750 °C, with a mass loss rate of 12–14 %, corresponding to both organic matter pyrolysis and mineral decomposition stage [47–50]. Although it is generally believed that the pyrolysis of organic matter occurs at a lower temperature than the mineral decomposition stage, there is some overlap in their temperature ranges [51]. For oil shales exhibiting single mass loss peaks for each stage (organic matter pyrolysis and mineral decomposition) [12,52–54], the temperature range for each stage can be determined based on the characteristics of the mass loss peaks. However, in the case of $OSC7_3$, overlapping mass loss peaks appear in the 300–750 °C range, indicating the occurrence of multiple pyrolysis reactions, which makes it difficult to distinguish the organic matter pyrolysis process accurately. As the heating rate increases from 0.5 °C/min to 4 °C/min, the overlapping mass loss peaks remain present, with an increase in both peak height and peak temperature. However, the relative shape of the peaks does not change significantly, suggesting that within this heating rate range, the pyrolysis process of the oil shale involves coupled multiple reactions. Therefore, deconvolution of the overlapping peaks in the DTG curves at each heating rate can be employed to decouple the multiple pyrolysis processes.

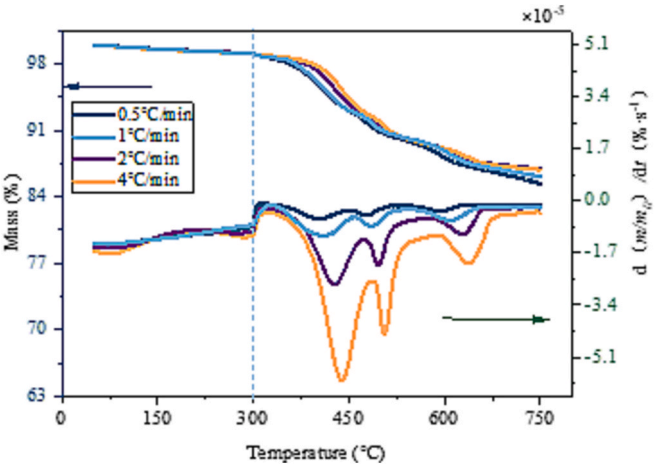

Fig. 3. TGA results of $OSC7_3$ pyrolysis at different heating rates.

According to the deconvolution method described in Section 2.2, the DTG curve of $OSC7_3$ at a heating rate of 0.5 °C/min was subjected to be deconvoluted with different numbers of fitted peaks. The selection range for the number of peaks was narrowed by comparing the fitting accuracy. The overlapping peaks within the 300–750 °C range, which correspond to multiple reaction processes, were selected for deconvolution. Based on previous work [30], the number of fitted peaks was defined to range from 3 to 7. The position and shape of the fitted peaks were iteratively adjusted using the algorithm provided by the Fityk software, until optimal fitting accuracy was achieved for each number of peaks. The fitting accuracy results for different numbers of peaks are shown in Table 3. It was observed that as the number of peaks increased, the fitting accuracy (R^2) improved from 0.9917 to 0.9994, and the residual sum of squares (*RSS*) decreased from 1.517E to 5 to 5.700E-7. The optimal number of peaks for achieving maximum fitting accuracy was determined to be 5, 6, and 7. Furthermore, the multi-peak fitting that best represents the actual reaction process was determined by

Table 3
Accuracy of fitting the DTG curve of oil shale pyrolysis at a heating rate of 0.5 °C/min using different numbers of fitted peaks.

Evaluation parameters	3 Peaks	4 Peaks	5 Peaks	6 Peaks	7 Peaks
R^2	0.9917	0.9964	0.9983	0.9983	0.9994
RSS	1.517E-5	6.596E-6	3.457E-6	3.599E-6	5.700E-7

evaluating the distributions of activation energies.

The DTG curves at heating rates of 0.5, 1, 2, and 4 °C/min were selected for peak deconvolution using three different numbers of peaks, and the activation energies were calculated for each case. As shown in Table 4, for the DTG curves at the four heating rates, all three peak fits exhibited good fitting accuracy.

The STK method was utilized to calculate the activation energy distributions of each reaction at conversions ranging from 0.1 to 0.9, employing various peak fits. The outcomes are depicted in Fig. 4. For the 5-peak fit, the average activation energies of the five reactions were determined to be 119.10, 295.68, 373.39, 962.31, and 403.20 kJ/mol, with relative standard deviations of 27.86 %, 18.90 %, 11.47 %, 4.56 %, and 6.95 %, respectively. The relative standard deviations of the activation energies for the first three reactions exceeded 20 %, making them unsuitable to be considered as distinct reactions. For the 7-peak fit, the average activation energies of the seven reactions were 181.08, 297.84, 352.84, 388.21, 348.74, 327.11, and 182.63 kJ/mol, with relative standard deviations of 8.17 %, 15.34 %, 5.42 %, 13.47 %, 10.99 %, 7.01 %, and 7.35 %, respectively. The relative standard deviations for the activation energies of the second, fourth, and fifth reactions exceeded 10 %. For the 6-peak fit, the average activation energies of the six reactions were 151.55, 212.30, 305.87, 359.14, 319.72, and 180.27 kJ/mol, with relative standard deviations of 9.98 %, 9.45 %, 9.67 %, 1.85 %, 3.79 %, and 4.93 %, respectively, all of which were less than 10 %. Therefore, the pyrolysis process of the $OSC7_3$ between 330 °C and 750 °C can be decoupled into six reactions.

Since the focus of in-situ conversion is on the pyrolysis of organic matter to produce oil and gas, it is necessary to identify the reactions involved in the pyrolysis of organic matter through the product distributions and reaction pathways of each reaction. At the same time, the kinetic model should be able to predict the product distributions. Before determining the product distributions of each reaction, it is necessary to establish the experimental temperature for each reaction based on its TG curve. This ensures that during staged isothermal pyrolysis experiments, only the appropriate reaction occurs at each temperature and that the products collected are fully representative of the reaction. Fig. 5 shows the 6-peak fitting results of the oil shale pyrolysis DTG curves at four different heating rates. From Fig. 5, it can be seen that although the heating rate affects the shape, temperature range, and peak temperature of each fitted peak, peaks with the same serial number have similar shapes, indicating that they correspond to the same reaction. The lower the heating rate, the easier it is to separate the different reactions and reduce their overlap. Therefore, only the DTG curve of the oil shale at a heating rate of 0.5 °C/min was analyzed. The temperature points for the staged isothermal pyrolysis experiments were determined from the peak temperatures of each fitted peak. The peak temperatures of the six reactions at this heating rate were 345 °C, 410 °C, 475 °C, 515 °C, 590 °C and 645 °C, with temperature ranges of 180–415 °C, 290–500 °C, 400–520 °C, 455–670 °C, 500–670 °C and 540–790 °C, respectively. These temperature ranges overlap, further confirming that the pyrolysis of the $OSC7_3$ is a coupled multiple reaction process. Among these, peak 2 has the largest area, corresponding to a weight loss of approximately 5 %, and represents the main pyrolysis reaction. Based on the weight loss characteristics of each reaction, staged isothermal pyrolysis experiments were carried out.

Table 4
The accuracy of fitting the DTG curves of oil shale pyrolysis at different heating rates using 5, 6, and 7 fitted peaks.

Heating rates / °C·min^{-1}	5 Peaks		6 Peaks		7 Peaks	
	R^2	*RSS*	R^2	*RSS*	R^2	*RSS*
0.5	0.9983	3.457E-6	0.9983	3.599E-6	0.9994	5.700E-7
1	0.9907	8.631E-6	0.9913	7.648E-6	0.9926	8.213E-7
2	0.9984	1.366E-6	0.9979	1.814E-6	0.9995	4.570E-7
4	0.9987	6.730E-7	0.9988	6.280E-7	0.9996	2.330E-7

3.2. Staged pyrolysis product distributions and pyrolysis mechanism of $OSC7_3$

In Section 3.1, the pyrolysis process of $OSC7_3$ was decoupled over the temperature range of 50–750 °C, dividing it into moisture evaporation and six distinct reactions. The peak temperatures for each reaction were identified as 345 °C, 410 °C, 475 °C, 515 °C, 590 °C, and 645 °C, respectively. To determine the product distributions and reaction pathways of each reaction, these six peak temperatures were selected as the temperature points for staged isothermal pyrolysis experiments. To avoid the accumulation of products from multiple reactions affecting the accuracy of the results, the oil shale samples were pyrolysed sequentially at each temperature point until no further product was released, considering the differences in reaction temperatures between each reaction. This approach ensured that the products obtained at each temperature point were exclusively derived from the corresponding distinct reaction. To account for water evaporation, 200 °C was added as the first temperature point for the staged isothermal experiments.

The staged isothermal pyrolysis experiments were conducted according to the above procedure, and the product distributions at each temperature point is shown in Fig. 6. At 200 °C, the water yield was 0.9 %, gas yield was 0.131 %, and oil yield was 0.08 %, with water being the dominant product, corresponding to the water evaporation process. At 345 °C, oil was the main product with a yield of 0.69 %, while gas and water yields were 0.363 % and 0.1 %, respectively. At 410 °C, total yield, oil yield, and gas yield all reached their peak values of 5.143 %, 2.82 %, and 1.923 %, respectively. The water yield was recorded at 0.4 %. This temperature corresponds to the most significant organic matter pyrolysis reaction. At 475 °C, oil yield was 0.78 %, gas yield was 1.017 %, and water yield dropped to 0.1 %, indicating another important oil and gas production reaction. At 515 °C, oil yield decreased to 0.1 %, while gas was the dominant product at 1.131 %, with water yield increasing to 0.4 %. No organic products were generated at 590 °C and 645 °C, suggesting that these temperatures and beyond correspond to the mineral decomposition stage.

In consideration of the heating cost limitations inherent to in-situ conversion technology, it is only necessary to attain temperatures sufficient to produce significant amounts of oil and gas from organic matter. There is no requirement to reach higher temperatures at which mineral decomposition occurs. Consequently, the mineral decomposition stage was not the focus of this study. Based on the product distributions at each temperature point, it was found that the total oil yield from $OSC7_3$ was approximately 4.47 %, and the total gas yield was about 4.535 %. The main oil-producing stages occurred at 345 °C, 410 °C, and 475 °C, with a combined oil yield of 4.37 %, while the primary gas-producing stages were at 410 °C, 475 °C, and 515 °C, with a combined gas yield of 4.071 %. The presence of oil products at 200 °C is attributed to the gradual initiation of the primary pyrolysis reaction at approximately 180 °C, and the oil and gas products observed at 200 °C are considered to be the result of reactions occurring at 345 °C. Thus, the organic matter pyrolysis process includes four key reactions at 345 °C, 410 °C, 475 °C, and 515 °C. Further analysis of the product composition and reaction pathways will be conducted through product characterization in subsequent studies.

The gas products generated at each temperature were analyzed using FTIR and GC, while the oil products and the solid products were characterized by GC–MS and XRD. The characteristic absorption bands of some gases and functional groups in the gas products [49,55–57] are summarized in **Table S2** in the supplementary material. XRD results indicate that no mineral decomposition occurs below 410 °C. Although mineral transformations are observed at 475 °C and 515 °C, their

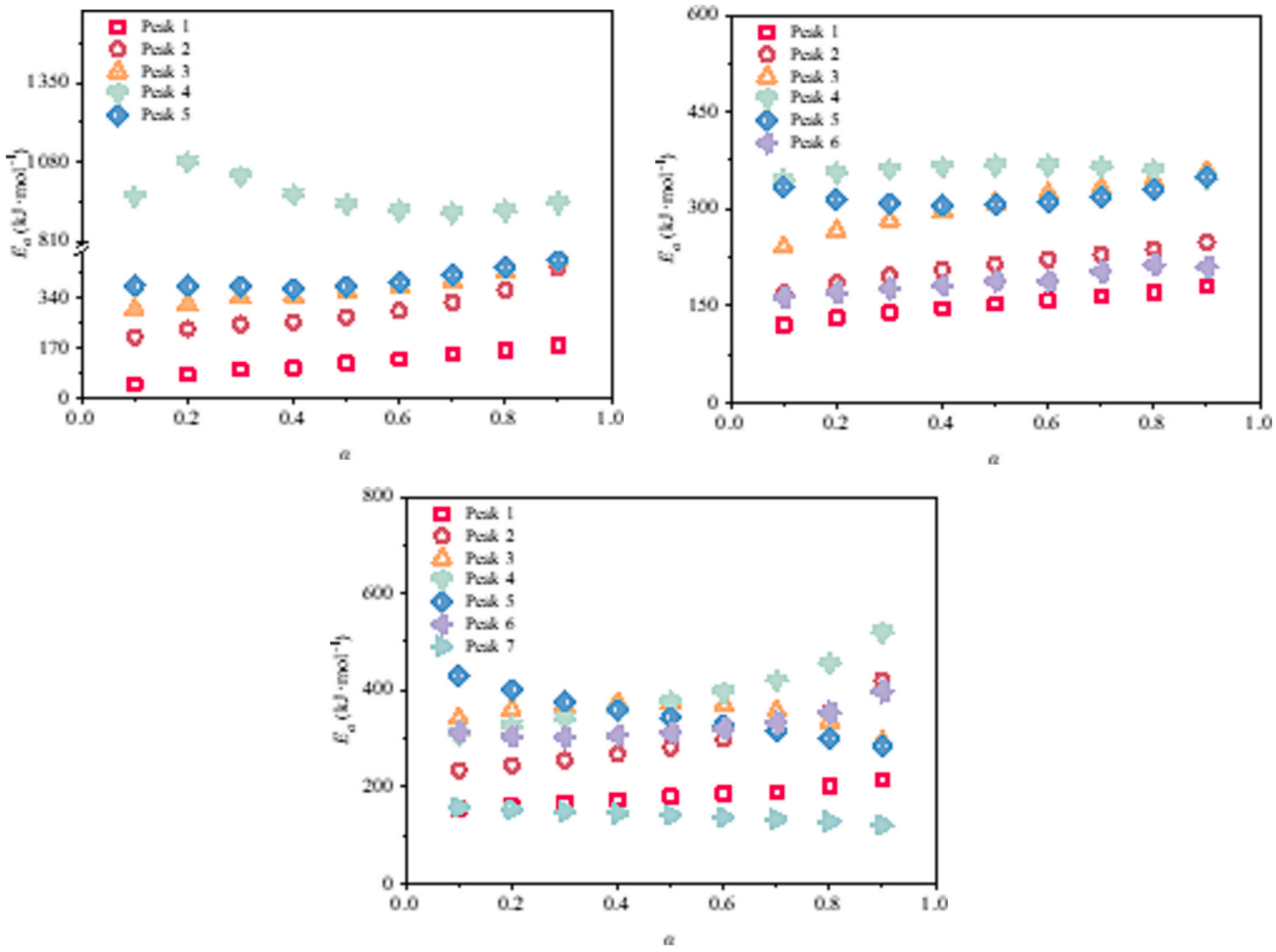

Fig. 4. Activation energy distributions of each peak corresponding to the reactions under (a) 5-peak fit; (b) 6-peak fit; and (c) 7-peak fit, as calculated by the STK method.

contribution to the overall mass loss of oil shale is negligible. Therefore, the thermal reactions occurring at 345 °C, 410 °C, 475 °C, and 515 °C are primarily attributed to the pyrolysis of organic matter, which is the main focus of in-situ conversion technology. Accordingly, detailed analyses of mineral decomposition processes are provided in the supplementary material. Detailed analysis results of the organic pyrolysis reactions are presented in Figs. 7 and 8, and Table 5.

At 345 °C, the organic matter (kerogen) in the oil shale began to react. Kerogen, which primarily consists of a carbon-based skeleton, contains various elements that form aliphatic, aromatic, and heteroatom-containing groups. These components are cross-linked into a complex, multi-layered network of chemical structures [58–60]. At this temperature, the water yield was only 0.1 %, the gas yield was 0.494 %, with amine gases and CO_2 as the main components, and the oil yield was 0.77 %. The oil products contained 71.83 % alkanes, 17.60 % heteroatomic compounds, 9.01 % cycloalkanes, 0.99 % alkenes, and 0.57 % aromatics. The alkanes were mainly distributed in the $C_{21\text{-}25}$ and C_{31+} carbon number ranges. The presence of amine gases, CO_2, and heteroatomic compounds indicates the breaking of weaker heteroatomic bonds, such as oxygen-bridged bonds, C-S, and C-N, in the kerogen [61]. The preponderance of alkanes, accompanied by a modest presence of cycloalkanes and alkenes, points to the degradation of aliphatic chains in proximity to aromatic rings and heteroatomic functional groups, culminating in the formation of more substantial molecular products. This observation indicates that kerogen undergoes depolymerization and transforms into bitumen [30,60]. Therefore, the first reaction in the process is the conversion of kerogen.

At 410 °C, since the sample had already been pyrolysed at 345 °C until no products were released, it indicates that the organic matter has fully transformed from kerogen into bitumen. Bitumen is a cage-like macromolecule rich in heteroatoms, with a central structure containing a large number of aromatic rings and other stable non-hydrocarbon forms, while the outer structure is predominantly linear, bonded to small molecules through non-covalent interactions [62]. Pyrolysis proceeds from the outer layers inward, with the outer linear chains initially degrading into aliphatic carbon chains [32,34,63], followed by cleavage of the inner stable structure [64]. At this temperature, oil yield was 2.82 %, with alkanes (56.56 %) and alkenes (23.98 %) as the primary products. The alkanes were mostly short-chain (C_{10}-C_{25}), with 16.69 % heteroatomic compounds and 2.77 % cycloalkanes. Gas yield was 1.923 %, with organic gases comprising 43 %, and H_2 and CO_2 accounting for 28 % and 29 %, respectively. Water yield was 0.4 %. The dominance of alkanes, alkenes, and H_2 suggests that the main reaction at this temperature involves the cleavage and dehydrogenation of weaker carbon chains in the outer bitumen layers [63,65]. The heteroatomic compounds were primarily alcohols, and the increased water yield indicates cleavage of hydroxyl groups and adjacent carbon chains. CO_2 and trace CO in the gas phase likely resulted from the cleavage of oxygen-containing functional groups such as carbonyl and ester groups [32,34]. These observations suggest that the weaker carbon chains on the outer layers of bitumen begin to break off at this temperature, indicating that the reaction pathway at this stage is the primary cracking

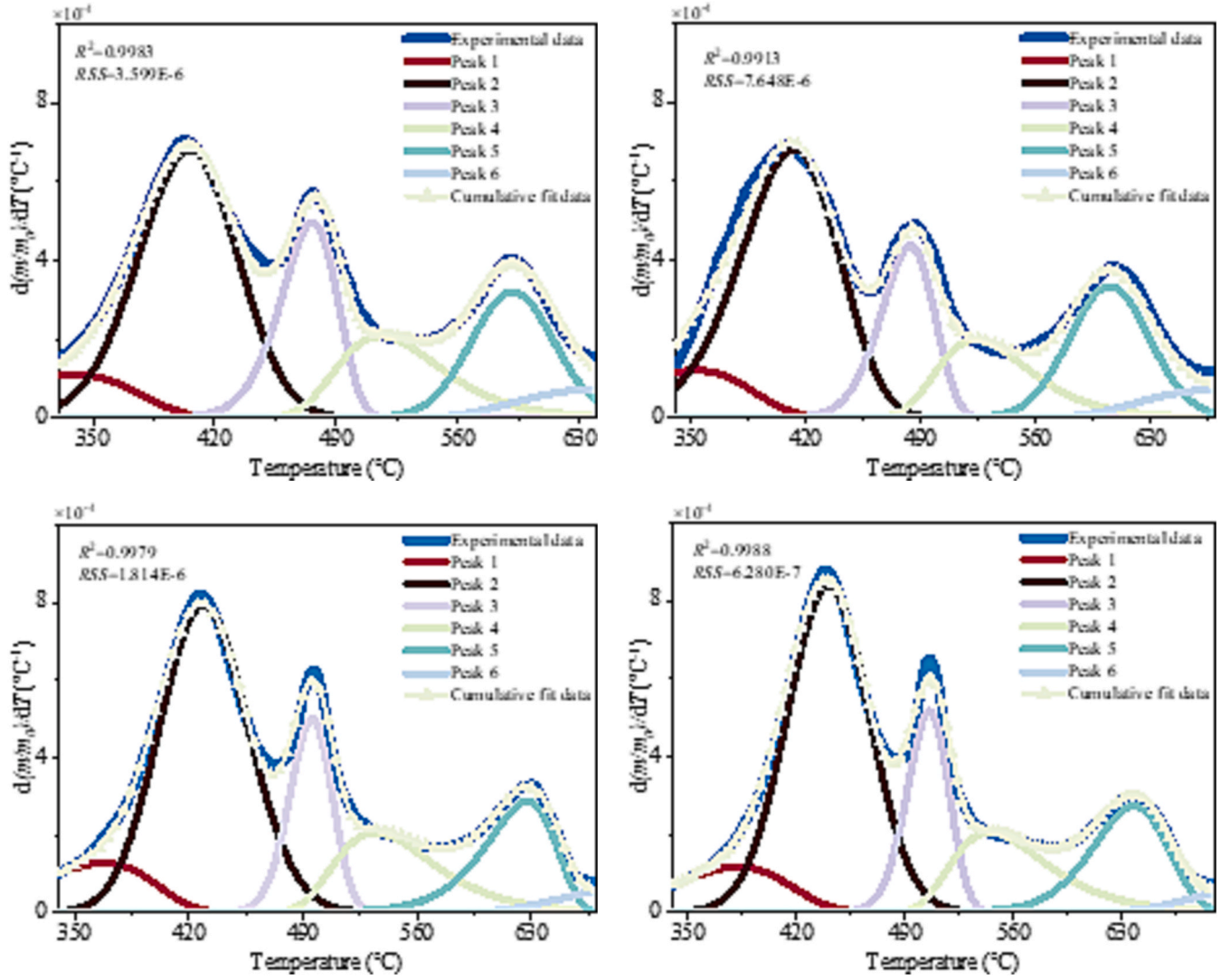

Fig. 5. Deconvolution of the DTG curves by 6-peak fit at a heating rate of (a) 0.5 °C/min; (b) 1 °C/min; (c) 2 °C/min; (d) 4 °C/min.

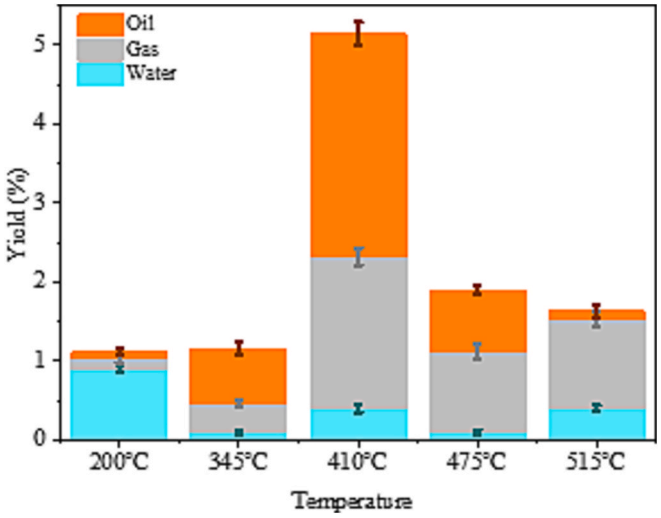

Fig. 6. Yields of oil, gas, and water products from staged isothermal pyrolysis of $OSC7_3$.

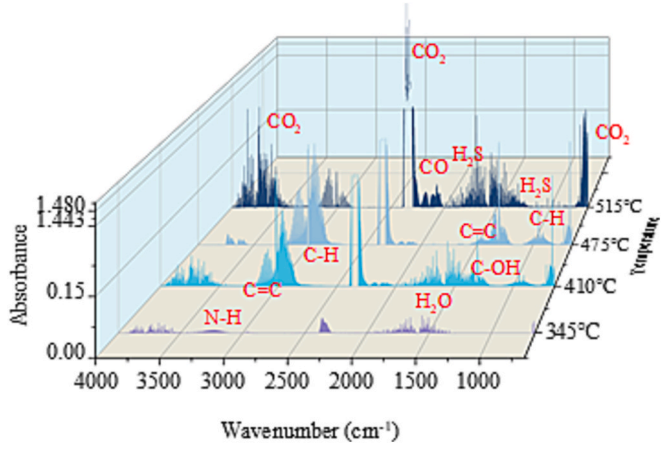

Fig. 7. FTIR spectra of gas products from staged isothermal pyrolysis of $OSC7_3$.

of bitumen, consistent with the pyrolysis mechanism observed in our previous work on the Nenjiang oil shale [30].

Before pyrolysis at 475 °C, bitumen had already lost some of its outer structure with lower bond energies. At this temperature, the gas yield

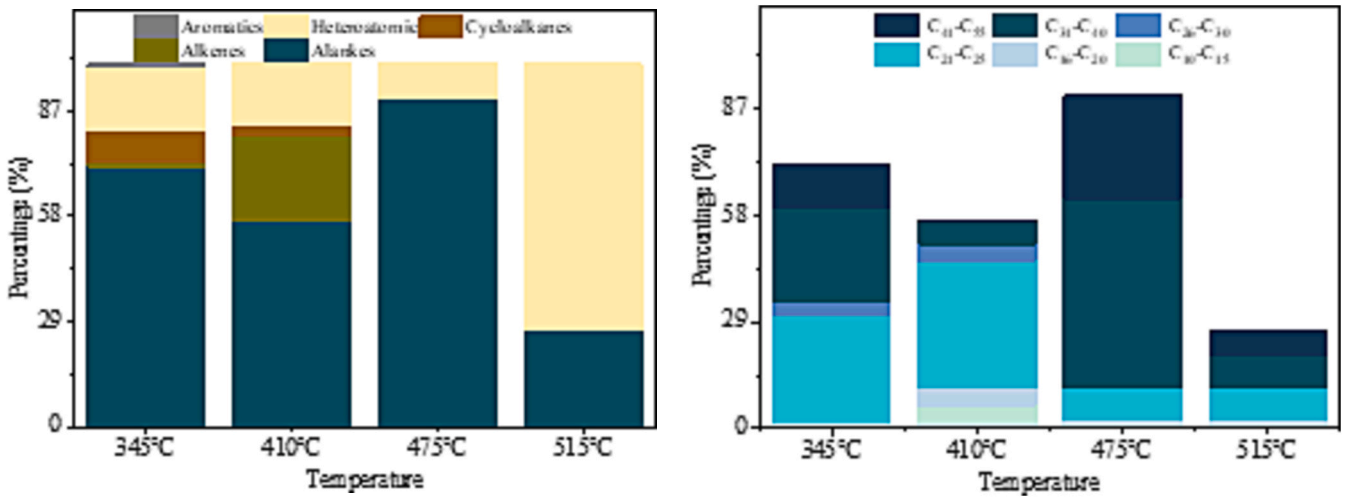

Fig. 8. Distributions of (a) oil products; and (b) alkane products from staged isothermal pyrolysis of $OSC7_3$.

Table 5
GC analysis of gas products from staged isothermal pyrolysis of $OSC7_3$.

	N_2/%	H_2/%	CO_2/%	C_1-C_4/%
345 °C	100			
410 °C	99.810	0.053	0.055	0.082
475 °C	99.754	0.067	0.061	0.118
515 °C	99.865	0.032	0.093	0.010

was 1.017 %, with a composition similar to 410 °C, but with a higher organic gas concentration (48 %), and the presence of 27 % H_2 and 25 % CO_2. The oil yield was 0.78 %, with 90.71 % alkanes (mostly C_{31+}), and 9.29 % alcohols. At this temperature, aliphatic compounds showed a polarized distribution, with more small molecular organic gases and large molecular alkanes, alongside significant H_2 production. This suggests the cracking of higher-carbon aliphatic chains in bitumen, forming larger alkanes. The higher temperature also cracks smaller oil products into aliphatic hydrocarbon gases. The presence of CO_2, CO, and alcohols in the oil products suggests further cleavage of oxygen-containing functional groups in the bitumen's outer structure. Thus, the reaction pathway at 475 °C is similar to 410 °C, but involves the breaking of higher-energy bonds in bitumen's outer structure, representing its secondary cracking. Both reactions primarily involve aliphatic hydrocarbons and hydroxyl-containing functional groups. This may be due to the higher content of aliphatic structures and oxygen functional groups in $OSC7_3$ kerogen [26,66]. The trace H_2S in the gas products likely originates from pyrite pyrolysis [67], as further supported by the XRD results in the supplementary material.

At 515 °C, gas products dominated with a yield of 1.131 %, where CO_2 content sharply increased to 69 %, while H_2 and organic gases accounted for 24 % and 7 %, respectively. The water yield increased to 0.4 %, and the oil yield was only 0.1 %, with 73.21 % of the oil products consisting of heteroatomic compounds, mostly containing oxygen, sulfur, nitrogen rings, and aromatic rings. The remaining oil products were alkanes, primarily with carbon numbers above C_{31}. The significant presence of CO_2 and heteroatom compounds at this temperature indicates the extensive cleavage of the more stable aromatic rings and non-hydrocarbon structures in bitumen. These functional groups, which are connected to benzene rings, have higher bond energies and can only be removed at high temperatures. Notably, the heteroatomic compounds contained a high proportion of nitrogen and sulfur rings, likely due to the higher nitrogen and sulfur content in the kerogen of $OSC7_3$ [62,67]. The limited quantity of organic gases in the gas products and the large molecular alkanes in the oil products correspond to the cracking of large carbon chains attached to benzene rings. Additionally, 24 % hydrogen in the gas phase may correspond to the condensation of benzene rings. Thus, this reaction represents the tertiary cracking of bitumen, primarily involving the cleavage of carbon chains near heteroatom-functionalized benzene rings and the condensation of benzene rings into carbon. The water product likely originates from the dehydration of clay minerals [51,68], which is evidenced by the changes in the shape of clay mineral diffraction peaks at 515 °C in the XRD results.

The results reveal the product composition and specific pathways of the four-step pyrolysis reactions of the organic matter in $OSC7_3$. In the first reaction process, kerogen transforms into bitumen, with weak bonds, such as those in heteroatomic functional groups, cracking to produce heteroatomic compounds and aliphatic hydrocarbons. In the second reaction process, the primary cracking of bitumen occurs, where weaker aliphatic carbon chains break and undergo dehydrogenation, generating alkanes, alkenes, and hydrogen. Oxygen-containing functional groups like hydroxyls also cleave, forming water, alcohol gases, CO_2, and CO. The third reaction involves the secondary cracking of bitumen, with large molecular aliphatic carbons further breaking down to form a significant number of alkanes (C_{31+}), as well as smaller alkanes and alkenes. Carbon chains near hydroxyl groups cleave, generating alcohols, while pyrite decomposition produces a small amount of H_2S. In the fourth reaction process, the tertiary cracking of bitumen occurs, with carbon chains near heteroatom-functionalized benzene rings breaking to generate a large number of heteroatom compounds. Most oxygen-containing functional groups cleave to produce CO_2, and benzene rings undergo condensation, resulting in carbon and H_2. Additionally, clay minerals undergo dehydration at this stage.

3.3. Organic matter pyrolysis kinetic model of $OSC7_3$

The generation of oil and gas is concentrated in the organic matter pyrolysis stage of oil shale. For $OSC7_3$, the pyrolysis process of its organic matter consists of four reactions: the conversion of kerogen, and the primary, second, and tertiary cracking of bitumen. By combining the results of the deconvolution integral peaks of the DTG curves at different heating rates with the product distributions of the four reactions, a kinetic model of organic matter cracking in this oil shale can be established which can accurately describe the organic matter cracking process and predict the product distributions.

The kinetic analysis of the four reactions was conducted using the method described in Section 2.4, with the resulting kinetic parameters presented in Table 6. The kinetic parameters were used to predict the reaction processes at four different heating rates, with the results shown in Table 7. The average prediction accuracy for each reaction at all four heating rates exceeded 0.9634. Notably, the kinetic parameters for

Table 6
Kinetic Parameters of the four pyrolysis reactions in the organic matter pyrolysis stage of $OSC7_3$.

Parameters	Reaction (1)	Reaction (2)	Reaction (3)	Reaction (4)
	Optimized values	Optimized values	Optimized values	Optimized values
E	175.769	233.664	324.611	353.943
A	9.02E + 12	6.27E + 15	5.14E + 20	8.73E + 20
C	1.2301	2.703	4.803	4.743
o	−0.9012	−0.159	−0.391	−0.612
n	1.5262	1.168	1.905	2.193
p	0.1182	−0.278	0.741	0.155

Table 7
Prediction accuracy of the kinetic equations for the four reactions at different heating rates.

	0.5℃/min	1℃/min	2℃/min	4℃/min	Average
Reaction (1)	0.9950	0.9923	0.9921	0.9550	0.9836
Reaction (2)	0.9858	0.9828	0.9396	0.9454	0.9634
Reaction (3)	0.9584	0.9335	0.9815	0.9868	0.9651
Reaction (4)	0.9380	0.9927	0.9775	0.9471	0.9638

reaction (1) (kerogen transformation) achieved an average prediction accuracy of 0.9836, indicating that the kinetic parameters for the four distinct reactions can accurately describe the occurrence of each independent reaction process.

After obtaining the kinetic parameters for each of the four reaction steps, the reaction kinetic equations and product distribution equations for these steps were established by combining the product distributions results from Section 3.2. These are presented in **Eqs. (16)–(19)**. In summarizing the product distributions of the four reactions, the gas products were classified based on GC results into organic gases (HC gases, C_1-C_4) and inorganic gases (Non-HC gases, primarily CO_2 and H_2). The liquid products were divided into four categories: heteroatomic compounds (NSO), alkanes with carbon numbers between C_{10}-C_{25} ($Sat_{10\text{-}25}$), alkanes with carbon numbers greater than C_{25} (Sat_{25+}), and unsaturated hydrocarbons (Unsat). Since the majority of unsaturated hydrocarbons have fewer than 25 carbon atoms, further classification of unsaturated hydrocarbons was not performed. In the product distribution equations, the coefficients represent the percentage yield of each product relative to the initial organic mass of the oil shale, which can be calculated from the shale mass and its TOC content.

Reaction (1)-The Conversion of kerogen:

$$\frac{d\alpha_1}{dt} = 9.02\times10^{12}\exp(-175.769/RT) \times 1.230\alpha^{-0.901}(1-\alpha)^{1.526}[-\ln(1-\alpha)]^{0.118} \quad (16)$$

$$Kerogen \rightarrow 0.703H_2O + 3.742Non-HCgases + 0.956NSO + 1.518Sat_{10-25} + 2.199Sat_{25+} + 0.569Unsat$$

$$\frac{d\alpha_2}{dt} = 6.27\times10^{15}\exp(-233.664/RT) \times 2.703\alpha^{-0.159}(1-\alpha)^{1.168}[-\ln(1-\alpha)]^{-0.278} \quad (17)$$

$$Bitumen \rightarrow 2.811H_2O + 5.833HCgases + 7.681Non-HCgases + 3.310NSO + 9.037Sat_{10-25} + 2.171Sat_{25+} + 5.299Unsat$$

$$\frac{d\alpha_3}{dt} = 5.14\times10^{20}\exp(-324.611/RT) \times 4.803\alpha^{-0.391}(1-\alpha)^{1.905}[-\ln(1-\alpha)]^{0.741}$$

$$Bitumen \rightarrow 0.703H_2O + 3.429HCgases + 3.717Non-HCgases + 0.513NSO + 0.597Sat_{10-25} + 4.378Sat_{25+} \quad (18)$$

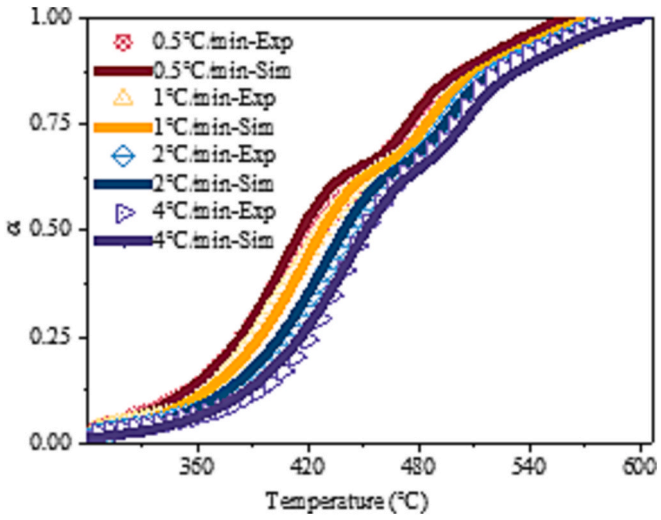

Fig. 9. Predicted $\alpha(T)$ curves of the organic matter pyrolysis stage in $OSC7_3$ at heating rates of 0.5–4 °C/min using the OMPM.

Reaction (4)-The tertiary cracking of bitumen:

$$\frac{d\alpha_4}{dt} = 8.73\times10^{20}\exp(-353.943/RT) \times 4.743\alpha^{-0.612}(1-\alpha)^{2.193}[-\ln(1-\alpha)]^{0.155}$$

$$Bitumen \rightarrow 2.811H_2O + 0.590HCgases + 7.358Non-HCgases + 0.513NSO + 0.077Sat_{10-25} + 0.112Sat_{25+} \quad (19)$$

By combining the kinetic equations for the four reactions according to **Eqs. (13)–(15)**, the OMPM can be established. The product distributions from the water evaporation stage to the organic matter pyrolysis stage of the $OSC7_3$ can be predicted using **Eq. (20)**.

$$Y_s = \sum_{l=1}^{4} Y_{s,l}\alpha_l$$

$$Y_W = \sum_{l=1}^{4} Y_{W,l}\alpha_l + Y_{W,W}\alpha_W \quad (20)$$

The subscript *s* represents the six categories of oil and gas products, including organic gases, inorganic gases, heteroatomic compounds, and others.

To validate the predictive accuracy of the OMPM for organic matter pyrolysis in the overall oil shale pyrolysis process, experimental and predicted conversion curves of oil shale organic matter at four heating rates were compared. These curves were calculated using **Eqs. (12) and (13)**, and the weight factors w_l for each reaction in **Eq. (13)** were determined based on **Eq. (14)** and the data from Fig. 6. The calculated weight factors were 0.130, 0.516, 0.190, and 0.164, respectively. The water yield $Y_{W,W}$ during the water evaporation stage was 0.9 %. For the conversion α_W during this stage, it was assumed that the conversion linearly increased from 0 to 1 between 50 °C and 300 °C, and remained at 1 after 300 °C.

Fig. 9 shows the predictive performance of the OMPM for the pyrolysis of $OSC7_3$ at heating rates of 0.5–4 °C/min. The results indicate that, within the temperature range of organic matter pyrolysis, the correlation coefficient (R^2) between the model's predictions and the experimental data exceeded 0.9984, demonstrating the high accuracy of the kinetic model in predicting the pyrolysis process within the 0.5–4 °C/min heating rate range.

The proposed kinetic model for organic matter pyrolysis stage in $OSC7_3$ effectively decouples the multi-step reactions and provides better guidance for the slow heating process during in-situ conversion of oil

shale. Therefore, we applied the OMPM, established using TGA result at heating rates of 0.5–4 °C/min, to predict the pyrolysis process at a slower heating rate of 0.2 °C/min. Additionally, product distributions at different temperature of $OSC7_3$ under 0.2 °C/min heating was obtained using **Eq. (20)**, with the results shown in Fig. 10. The model achieved a high prediction accuracy of 0.9927 for the pyrolysis process at 0.2 °C/min, indicating that the accurate decoupling of the pyrolysis process allows the model to be applied to predict slower pyrolysis processes. This result validates the reliability of the proposed kinetic modeling approach. Fig. 10(b) presents the product yield curves for seven categories of products as a function of temperature. Two main stages of oil and gas yield growth can be observed: the first stage, between 250–420 °C, where oil and gas yields increased to 3.7 % and 2.5 %, respectively. During this stage, the yields of all types of oil and gas products increased, with small molecular saturated and unsaturated hydrocarbons being the major products, contributing to a total yield of 3 %. The second stage, between 420–530 °C, saw oil and gas yields reach 4.47 % and 4.54 %, respectively. In this stage, the oil products consisted more of large molecular alkanes and heteroatomic compounds, accounting for a total yield of 2.06 %, while inorganic gases increased in the gas phase, with a yield of 3.14 %. As discussed in Section 3.2, the CO_2 yield in this stage increased sharply, which could potentially lead to reduced extraction efficiency. Based on the product composition in different stages, the heating temperature can be adjusted according to the balance between extraction yield and heating cost. Thus, this work successfully decouples the multi-step pyrolysis process of $OSC7_3$, elucidates the product distributions and reaction pathways for each stage, and establishes an accurate kinetic model, providing valuable insights for the development of in-situ conversion technology.

4. Conclusion

To better predict the slow pyrolysis process and product distributions of oil shale in in-situ conversion, this study proposes a kinetic modeling approach for organic matter pyrolysis. TGA was first used to obtain the pyrolysis characteristics of oil shale. The peak deconvolution method and activation energy analysis were then applied to decouple the pyrolysis process into multiple reactions. Staged isothermal pyrolysis experiments were conducted to determine product distributions and pathways for each reaction. Finally, a kinetic model was developed to accurately describe the pyrolysis process and predict product distributions. This approach was applied to $OSC7_3$, leading to the following conclusions.

The temperature-programmed pyrolysis experiments showed that, at heating rates of 0.5–4 °C/min, $OSC7_3$ exhibited overlapping weight loss peaks after 330 °C, indicating the coupling of multiple reactions. Using peak deconvolution, the highest fitting accuracy was achieved for the 5th, 6th, and 7th peaks. The STK method revealed that the 6-peak fitting yielded the smallest relative standard deviation of activation energy for each peak, all below 10 %. As a result, the pyrolysis process from 50 °C to 750 °C was decoupled into six reactions, with peak temperatures at 345 °C, 410 °C, 475 °C, 515 °C, 590 °C, and 645 °C.

Staged isothermal pyrolysis experiments were conducted on $OSC7_3$, using temperature points at 200 °C (for water evaporation) and the peak temperatures of each reaction. The product distribution results show that organic oil and gas are primarily produced in the first four reactions. For $OSC7_3$, the total oil yield was approximately 4.42 %, and the gas yield was about 4.505 %. Based on oil and gas characterization, the product distributions and reaction pathways for the four reactions were determined: In the first reaction process, kerogen is converted to bitumen, with cleavage of weak bonds, such as heteroatomic functional groups. In the second reaction process, bitumen undergoes primary cracking, with dehydrogenation of weaker aliphatic carbons and cleavage of oxygen-containing groups like hydroxyls. As the process continues, bitumen undergoes secondary cracking, where larger molecular aliphatic carbons further break down, and carbon chains near hydroxyl groups cleave. Finally, the tertiary cracking of bitumen occurs, where carbon chains near heteroatomic functional groups connected to benzene rings break, leading to the cleavage of most oxygen-containing functional groups. Benzene rings also polymerize at this stage, and clay minerals dehydrate.

Kinetic analysis was conducted using the deconvolution results of the DTG curves at heating rates of 0.5, 1, 2, and 4 °C/min, and kinetic equations were derived for the four reactions. The prediction accuracy for each reaction exceeded 0.96. By integrating the product distributions, the OMPM was developed. The OMPM accurately predicted the pyrolysis process at heating rates of 0.5–4 °C/min, with a fitting accuracy greater than 0.9984. The OMPM was also applied to predict the pyrolysis process at a slower heating rate (0.2 °C/min), achieving a prediction accuracy of 0.9927. This suggests that the accurate decoupling of the pyrolysis process allows the established kinetic model to effectively predict slower pyrolysis behaviors. The predicted product distributions show that the increase in oil and gas yields occurs in two main stages. By analyzing the product composition at each stage, heating temperatures can be adjusted based on a balance between extraction yields and heating costs.

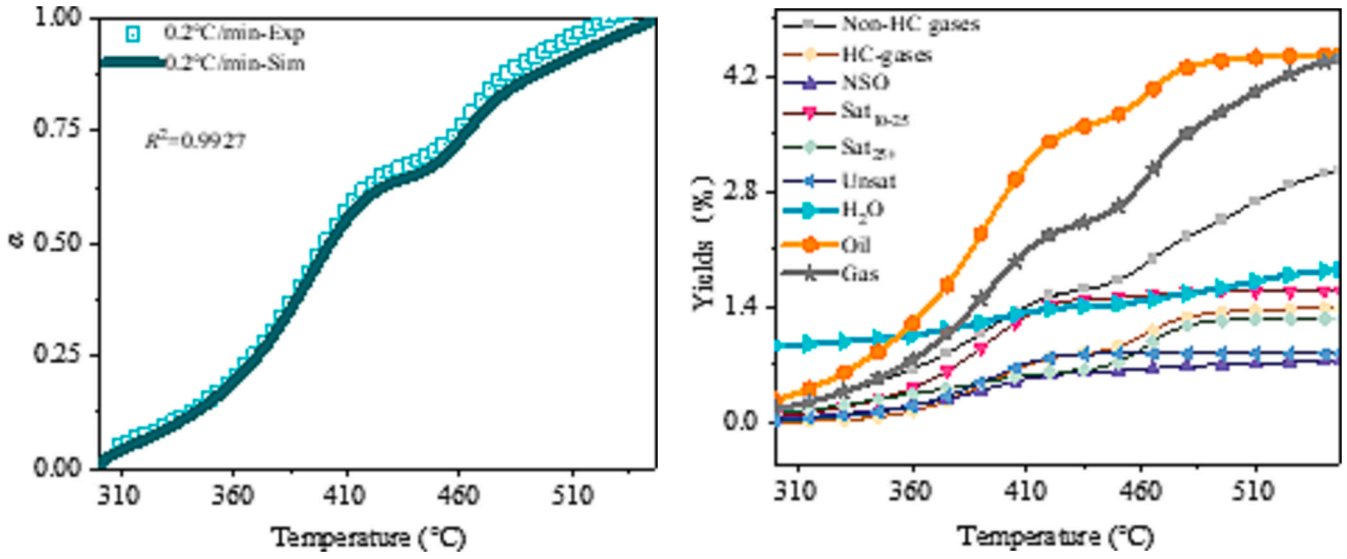

Fig. 10. Prediction of the conversion (a) and product distributions (b) for organic matter pyrolysis of $OSC7_3$ at 0.2 °C/min using the OMPM.

The proposed kinetic modeling approach for organic matter pyrolysis is effective in accurately predicting the slow pyrolysis behavior and product distributions of oil shale in the in-situ conversion process, providing valuable guidance for the development of in-situ conversion technology.

CRediT authorship contribution statement

Chi Xiong: Writing – original draft, Visualization, Software, Methodology, Investigation, Formal analysis, Conceptualization. **Jingyu Chen:** Writing – review & editing, Methodology, Investigation. **Ruina Xu:** Validation, Resources, Project administration, Methodology, Funding acquisition. **Qiang Song:** Writing – review & editing, Supervision, Project administration, Funding acquisition.

Declaration of competing interest

The authors declare that they have no known competing financial interests or personal relationships that could have appeared to influence the work reported in this paper.

Acknowledgements

This research is financially supported by the National Natural Science Foundation of China (U22B6004) and the Fundamental Research Funds for the Central Universities of China (2022ZFJH04).

Appendix A. Supplementary material

Supplementary data to this article can be found online at https://doi.org/10.1016/j.enconman.2025.120096.

Data availability

Data will be made available on request.

References

[1] Hu S, Zhao W, Hou L, Yang Z, Zhu R, Wu S, et al. Development potential and technical strategy of continental shale oil in China. Pet Explor Dev 2020;47:877–87. https://doi.org/10.1016/S1876-3804(20)60103-3.
[2] Zhao W, Hu S, Hou L. Connotation and strategic role of in-situ conversion processing of shale oil underground in the onshore China. Pet Explor Dev 2018;45:563–72. https://doi.org/10.1016/S1876-3804(18)30063-6.
[3] Zhao W, Hu S, Hou L, Yang T, Li X, Guo B, et al. Types and resource potential of continental shale oil in China and its boundary with tight oil. Pet Explor Dev 2020;47:1–11. https://doi.org/10.1016/S1876-3804(20)60001-5.
[4] Zou C, Pan S, Jing Z, et al. Shale oil and gas revolution and its impact. Acta Pet Sin 2020;41:1–12. https://doi.org/10.7623/syxb202001001.
[5] Jin Z, Zhu R, Liang X, Shen Y. Several issues worthy of attention in current lacustrine shale oil exploration and development. Pet Explor Dev 2021;48:1471–84. https://doi.org/10.1016/S1876-3804(21)60303-8.
[6] Li S, Li X, Wang S, et al. Theory and method of in-situ conversion of shale oil by chemical thermal. J Eng Geol 2022;30:127–43. https://doi.org/10.13544/j.cnki.jeg.2021-0796.
[7] Li S, Yue C. Study of pyrolysis kinetics of oil shale. Fuel 2003;82:337–42. https://doi.org/10.1016/S0016-2361(02)00268-5.
[8] Bai F, Guo W, Lü X, Liu Y, Guo M, Li Q, et al. Kinetic study on the pyrolysis behavior of Huadian oil shale via non-isothermal thermogravimetric data. Fuel 2015;146:111–8. https://doi.org/10.1016/j.fuel.2014.12.073.
[9] Bai F, Sun Y, Liu Y, Guo M, Zhao J. Characteristics and kinetics of huadian oil shale pyrolysis via non-isothermal thermogravimetric and gray relational analysis. Combust Sci Technol 2020;192:471–85. https://doi.org/10.1080/00102202.2019.1576650.
[10] Moine EC, Bouamoud R, El Hamidi A, Khachani M, Halim M, Arsalane S. Mineralogical characterization and non-isothermal pyrolysis kinetics of Moroccan Rif oil shale. J Therm Anal Calorim 2018;131:993–1004. https://doi.org/10.1007/s10973-017-6632-6.
[11] Pan N, Li D, Lü W, Dai F. Kinetic study on the pyrolysis behavior of Jimsar oil shale. Oil Shale 2019;36(4):462–82. https://doi.org/10.3176/oil.2019.4.02.
[12] Liu Q, Han X, Li Q, Huang Y, Jiang X. TG–DSC analysis of pyrolysis process of two Chinese oil shales. J Therm Anal Calorim 2014;116:511–7. https://doi.org/10.1007/s10973-013-3524-2.
[13] Abu El-Rub Z, Kujawa J, Al-Gharabli S. Pyrolysis kinetic parameters of Omari oil shale using thermogravimetric analysis. Energies 2020;13:4060. https://doi.org/10.3390/en13164060.
[14] Zhao S, Su J, Wu J. Release performance and kinetic behavior of volatile products from controlled pressure pyrolysis of oil shale in nitrogen atmosphere. Sci Rep 2023;13:10676. https://doi.org/10.1038/s41598-023-37459-5.
[15] Sütcü H. Pyrolysis kinetics of oil shale from Urukisla. Turkey Oil Shale 2009;26(4):491–9. https://doi.org/10.3176/oil.2009.4.05.
[16] Baruah B, Kataki R, Thakur P, Tiwari P. Detailed physicochemical and thermochemical investigation of Upper Assam oil shale. J Therm Anal Calorim 2019;138:1221–32. https://doi.org/10.1007/s10973-019-08163-2.
[17] Zhang J, Ding Y, Du W, Lu K, Sun L. Study on pyrolysis kinetics and reaction mechanism of Beizao oil shale. Fuel 2021;296:120696. https://doi.org/10.1016/j.fuel.2021.120696.
[18] Bai F, Sun Y, Liu Y, Li Q, Guo M. Thermal and kinetic characteristics of pyrolysis and combustion of three oil shales. Energ Conver Manage 2015;97:374–81. https://doi.org/10.1016/j.enconman.2015.03.007.
[19] Hua Z, Wang Q, Jia C, Liu Q. Pyrolysis kinetics of a Wangqing oil shale using thermogravimetric analysis. Energy Sci Eng 2019;7:912–20. https://doi.org/10.1002/ese3.320.
[20] Jiang H, Liu S, Wang J, You Y, Yuan S. Study on evolution mechanism of the pyrolysis of chang 7 oil shale from Ordos basin in China. Energy 2023;272:127097. https://doi.org/10.1016/j.energy.2023.127097.
[21] Ryan RC, Fowler TD, Beer GL, Nair V, Ogunsola OI, Hartstein AM, Ogunsola O. Shell's in situ conversion process—from laboratory to field pilots. In: Oil Shale: A Solution to the Liquid Fuel Dilemma, ACS Symposium Series 1032; American Chemical Society: Washington DC, 2010.
[22] Park DK, Song E. Pyrolysis and char oxidation characteristics of oil shales and coal in a thermogravimetric analyzer. Can J Chem Eng 2017;95:2367–73. https://doi.org/10.1002/cjce.22894.
[23] Syed S, Qudaih R, Talab I, Janajreh I. Kinetics of pyrolysis and combustion of oil shale sample from thermogravimetric data. Fuel 2011;90:1631–7. https://doi.org/10.1016/j.fuel.2010.10.033.
[24] Vyazovkin S, Burnham AK, Favergeon L, Koga N, Moukhina E, Pérez-Maqueda LA, et al. ICTAC Kinetics Committee recommendations for analysis of multi-step kinetics. Thermochim Acta 2020;689:178597. https://doi.org/10.1016/j.tca.2020.178597.
[25] Ding H, Ma Y, Li S, Wang Q, Hong W, Jiang H, et al. Pyrolytic characteristics of Fushun oil shale and its by-products. J Therm Anal Calorim 2022;147:5255–67. https://doi.org/10.1007/s10973-021-10870-8.
[26] You Y, Han X, Liu J, Jiang X. Structural characteristics and pyrolysis behaviors of huadian oil shale kerogens using solid-state 13C NMR, Py-GCMS and TG. J Therm Anal Calorim 2018;131:1845–55. https://doi.org/10.1007/s10973-017-6667-8.
[27] Hu M, Chen Z, Wang S, Guo D, Ma C, Zhou Y, et al. Thermogravimetric kinetics of lignocellulosic biomass slow pyrolysis using distributed activation energy model, Fraser-Suzuki deconvolution, and iso-conversional method. Energy Conv Manag 2016;118:1–11. https://doi.org/10.1016/j.enconman.2016.03.058.
[28] Bhaduri A, Gupta A, Olivier A, Graham-Brady L. An efficient optimization based microstructure reconstruction approach with multiple loss functions. Comput Mater Sci 2021;199:110709. https://doi.org/10.1016/j.commatsci.2021.110709.
[29] Alves JLF, da Silva JCG, Mumbach GD, Di Domenico M, Marangoni C. Assessing the potential of the invasive grass Cenchrus echinatus for bioenergy production: a study of its physicochemical properties, pyrolysis kinetics and thermodynamics. Thermochim Acta 2023;724:179500. https://doi.org/10.1016/j.tca.2023.179500.
[30] Xiong C, Chen J, Xu R, Song Q. Pyrolysis characteristics and mechanism of oil shale in the Songliao Basin of China. Fuel 2025;386:134251. https://doi.org/10.1016/j.fuel.2024.134251.
[31] Zhang H, Wang S, Shi C, Yan J, Ge X, Shen J, et al. Evolution characteristics of products retorted from Gonghe oil shale based on TG-FTIR and Py-GC/MS. Thermochim Acta 2022;716:179325. https://doi.org/10.1016/j.tca.2022.179325.
[32] You Y, Han X, Wang X, Jiang X. Evolution of gas and shale oil during oil shale kerogen pyrolysis based on structural characteristics. J Anal Appl Pyrol 2019;138:203–10. https://doi.org/10.1016/j.jaap.2018.12.025.
[33] Qing W, Xinmin W, Shuo P. Study on the structure, pyrolysis kinetics, gas release, reaction mechanism, and pathways of Fushun oil shale and kerogen in China. Fuel Process Technol 2022;225:107058. https://doi.org/10.1016/j.fuproc.2021.107058.
[34] Chen B, Han X, Li Q, Jiang X. Study of the thermal conversions of organic carbon of Huadian oil shale during pyrolysis. Energ Conver Manage 2016;127:284–92. https://doi.org/10.1016/j.enconman.2016.09.019.
[35] Yang Y, Liu Y, Zhou D, Jiao X, Cao Q, Meng Z, et al. Lithotypes, organic matter and paleoenvironment characteristics in the Chang73 submember of the Triassic Yanchang Formation, Ordos Basin, China: implications for organic matter accumulation and favourable target lithotype. J Pet Sci Eng 2022;216:110691. https://doi.org/10.1016/j.petrol.2022.110691.
[36] Starink MJ. The determination of activation energy from linear heating rate experiments: a comparison of the accuracy of isoconversion methods. Thermochim Acta 2003;404:163–76. https://doi.org/10.1016/S0040-6031(03)00144-8.
[37] Coats AW, Redfern JP. Kinetic parameters from thermogravimetric data. Nature 1964;201:68–9. https://doi.org/10.1038/201068a0.
[38] Friedman HL. Kinetics of thermal degradation of char-forming plastics from thermogravimetry. Application to a phenolic plastic. J Polym Sci, Part C: Polym Symp 1964;6:183–95. https://doi.org/10.1002/polc.5070060121.
[39] Vyazovkin S, Burnham AK, Criado Luque JM, Pérez-Maqueda LA, Popescu C, Sbirrazzuoli N. ICTAC Kinetics Committee recommendations for performing kinetic computations on thermal analysis data 2011. doi: 10.1016/j.tca.2011.03.034.

[40] Khawam A, Flanagan DR. Solid-state kinetic models: basics and mathematical fundamentals. J Phys Chem B 2006;110:17315–28. https://doi.org/10.1021/jp062746a.
[41] Bai F, Liu Y, Lai C, Sun Y, Wang J, Sun P, et al. Thermal degradations and processes of four kerogens via thermogravimetric–fourier-transform infrared: pyrolysis performances, products, and kinetics. Energy Fuels 2020;34:2969–79. https://doi.org/10.1021/acs.energyfuels.9b04231.
[42] Aboulkas A, El Harfi K. Study of the kinetics and mechanisms of thermal decomposition of Moroccan Tarfaya oil shale and its Kerogen. Oil Shale 2008;25:426. https://doi.org/10.3176/oil.2008.4.04.
[43] Zhang Z, Duan H, Zhang Y, Guo X, Yu X, Zhang X, et al. Investigation of kinetic compensation effect in lignocellulosic biomass torrefaction: kinetic and thermodynamic analyses. Energy 2020;207:118290. https://doi.org/10.1016/j.energy.2020.118290.
[44] Mumbach GD, Alves JLF, da Silva JCG, Domenico MD, Arias S, Pacheco JGA, et al. Prospecting pecan nutshell pyrolysis as a source of bioenergy and bio-based chemicals using multicomponent kinetic modeling, thermodynamic parameters estimation, and Py-GC/MS analysis. Renew Sustain Energy Rev 2022;153:111753. https://doi.org/10.1016/j.rser.2021.111753.
[45] Rani S, Saksham S, Sharma J, Padmanabhan E, Sathiavelu S. Characterizing pyrolysis behavior and kinetic parameters of shale using thermogravimetry. Arab J Geosci 2022;15:123. https://doi.org/10.1007/s12517-021-09389-x.
[46] Jaber JO, Probert SD. Non-isothermal thermogravimetry and decomposition kinetics of two Jordanian oil shales under different processing conditions. Fuel Process Technol 2000;63:57–70. https://doi.org/10.1016/S0378-3820(99)00064-8.
[47] Sonibare OO, Ehinola OA, Egashira R. Thermal and geochemical characterization of Lokpanta oil shales Nigeria. Energy Conv Manag 2005;46:2335–44. https://doi.org/10.1016/j.enconman.2005.01.001.
[48] Sun Y, Bai F, Liu B, Liu Y, Guo M, Guo W, et al. Characterization of the oil shale products derived via topochemical reaction method. Fuel 2014;115:338–46. https://doi.org/10.1016/j.fuel.2013.07.029.
[49] Fan C, Yan J, Huang Y, Han X, Jiang X. XRD and TG-FTIR study of the effect of mineral matrix on the pyrolysis and combustion of organic matter in shale char. Fuel 2015;139:502–10. https://doi.org/10.1016/j.fuel.2014.09.021.
[50] Bouamoud R, Moine EC, Mulongo-Masamba R, El Hamidi A, Halim M, Arsalane S. Type I kerogen-rich oil shale from the Democratic Republic of the Congo: mineralogical description and pyrolysis kinetics. Pet Sci 2020;17:255–67. https://doi.org/10.1007/s12182-019-00384-2.
[51] Berkovich AJ, Young BR, Levy JH, Schmidt SJ. Thermal characterisation of Australian oil shales. J Therm Anal 1997;49:737–43.
[52] Jiang XM, Han XX, Cui ZG. Mechanismand mathematical model of huadian oil shale pyrolysis. J Therm Anal Calorim 2006;86:457–62. https://doi.org/10.1007/s10973-005-7065-1.
[53] Huang Y, Fan C, Han X, Jiang X. A TGA-MS investigation of the effect of heating rate and mineral matrix on the pyrolysis of kerogen in oil shale. Oil Shale 2016;33:125. https://doi.org/10.3176/oil.2016.2.03.
[54] Han J, Sun Y, Guo W, Deng S, Hou C, Qu L, et al. Non-isothermal thermogravimetric analysis of pyrolysis kinetics of four oil shales using Sestak–Berggren method. J Therm Anal Calorim 2019;135:2287–96. https://doi.org/10.1007/s10973-018-7392-7.
[55] Liu Z, Ma H, Guo J, Liu G, Wang Z, Guo Y. Pyrolysis characteristics and effect on pore structure of Jimsar oil shale based on TG-FTIR-MS analysis. Geofluids 2022;2022:e7857239. https://doi.org/10.1155/2022/7857239.
[56] Lu H, Pan L, Chen P, Liu T. Research on the characteristics and kinetics of the pyrolysis process and products generation of jimsar (China) oil shale using TG-FTIR. Processes 2023;11:1535. https://doi.org/10.3390/pr11051535.
[57] Farobie O, Amrullah A, Syaftika N, Bayu A, Hartulistiyoso E, Fatriasari W, et al. Valorization of rejected macroalgae kappaphycopsis cottonii for bio-oil and biochar production via slow pyrolysis. ACS Omega 2024;9:16665–75. https://doi.org/10.1021/acsomega.4c00678.
[58] Liu X, Zhan J-H, Lai D, Liu X, Zhang Z, Xu G. Initial pyrolysis mechanism of oil shale kerogen with reactive molecular dynamics simulation. Energy Fuels 2015;29:2987–97. https://doi.org/10.1021/acs.energyfuels.5b00084.
[59] Qian Y, Zhan J-H, Lai D, Li M, Liu X, Xu G. Primary understanding of non-isothermal pyrolysis behavior for oil shale kerogen using reactive molecular dynamics simulation. Int JHydrogen Energy 2016;41:12093–100. https://doi.org/10.1016/j.ijhydene.2016.05.106.
[60] Wang Y, Han X, Jiang X. Exploring pyrolysis of the aromatics in shale oil by experimental study and kinetic modelling. Energy 2023;279:127998. https://doi.org/10.1016/j.energy.2023.127998.
[61] Ru X, Cheng Z, Song L, Wang H, Li J. Experimental and computational studies on the average molecular structure of Chinese Huadian oil shale kerogen. J Mol Struct 2012;1030:10–8. https://doi.org/10.1016/j.molstruc.2012.07.027.
[62] Wu J, Fang P, Wang X-C, Li B, Liu K, Ma X, et al. The potential occurrence modes of hydrocarbons in asphaltene matrix and its geochemical implications. Fuel 2020;278:118233. https://doi.org/10.1016/j.fuel.2020.118233.
[63] Lai D, Zhan J-H, Tian Y, Gao S, Xu G. Mechanism of kerogen pyrolysis in terms of chemical structure transformation. Fuel 2017;199:504–11. https://doi.org/10.1016/j.fuel.2017.03.013.
[64] Ding H, Ma Y, Li S, Wang Q, Hong W, Jiang H, et al. Pyrolysis characteristics of oil shale semi-coke and its extracted bitumen. J Anal Appl Pyrol 2021;156:105120. https://doi.org/10.1016/j.jaap.2021.105120.
[65] Wu Z, Xu Z. Experimental and molecular dynamics investigation on the pyrolysis mechanism of Chang 7 type-II oil shale kerogen. J Pet Sci Eng 2022;209:109878. https://doi.org/10.1016/j.petrol.2021.109878.
[66] Guo H, Jia W, Peng P, Lei Y, Luo X, Cheng M, et al. The composition and its impact on the methane sorption of lacustrine shales from the Upper Triassic Yanchang Formation, Ordos Basin China. Mar Petrol Geol 2014;57:509–20. https://doi.org/10.1016/j.marpetgeo.2014.05.010.
[67] Gai R, Jin L, Zhang J, Wang J, Hu H. Effect of inherent and additional pyrite on the pyrolysis behavior of oil shale. J Anal Appl Pyrol 2014;105:342–7. https://doi.org/10.1016/j.jaap.2013.11.022.
[68] Ge Z, Sun Q, Li D, Shi Q, Wei S, Yang T. Pyrolysis characteristics of organic-rich shale from the Chang 7 member of Triassic Yanhe Profile in Ordos Basin. Arab J Geosci 2021;14:1024. https://doi.org/10.1007/s12517-021-07382-y.